Operando Optical Microscopy of Dead Lithium Growth in Anode-Less Configuration

Martina Romio, Jürgen Kahr, Ermanno Miele, Martin Krammer, Yuri Surace, Buket Boz, Palanivel Molaiyan, Theodoros Dimopoulos, Michel Armand,* and Andrea Paolella*

There is an increasing demand to improve battery safety and performance as part of the global push to convert the small electronics and transportation sector to infrastructures based on electricity. This work follows the deposition of lithium metal in anode-less conditions by an *operando* optical microscope using a transparent indium tin oxide-polyethylene terephthalate (ITO-PET) window as the current collector in a readily-available electrochemical set-up. The mechanism of Li metal nucleation strongly depends on the selected current densities (C/40 and 2C). After the deposition of the solid electrolyte interface (SEI), Li nucleates from mossy to needle morphology. Moreover, layer-by-layer growth of dead Li in voids is monitored by following its accumulation upon cycling. Dead Li deposits in residual hollow structures, especially when high current densities are applied. These optical observations are coupled with computer vision analyses to evaluate the average size of the Li deposits: smaller Li nuclei plate when high C-rate is applied. The results here described provide insights into a new electrochemical cell concept that enables to elucidate the influence of spatial inhomogeneities of the lithophilic ITO-PET surface on the mechanism of Li nucleation and plating.

M. Romio, J. Kahr, Y. Surace, B. Boz, P. Molaiyan
Battery Technologies
Austrian Institute of Technology
Giefinggasse 2, Vienna 1210, Austria
E. Miele
Department of Physics
Cavendish Laboratory
University of Cambridge
Nanophotonics Centre, Cambridge CB3 0HE, UK
M. Krammer, T. Dimopoulos
Energy Conversion and Hydrogen
Austrian Institute of Technology
Giefinggasse 2, Vienna 1210, Austria
M. Armand
CIC Energigune Parque Tecnológico de Álava Albert Einstein 48
Vitoria-Gasteiz, Álava 01510, Spain
E-mail: marmand@cicenergigune.com
A. Paolella
Dipartimento di Scienze Chimiche e Geologiche
Università degli Studi di Modena e Reggio Emilia
Via Campi 103, Modena 41125, Italy
E-mail: andrea.paolella@unimore.it

1. Introduction

Electrochemical energy storage systems, specifically lithium-ion batteries (LIBs), are ubiquitous in contemporary society with the widespread usage and demand of portable electronic devices and electric vehicles.[1,2] Now more than ever before, energy storage devices are required to have improved safety standards along with high capacity and energy density.[3] Therefore, a lithium metal foil is considered a promising anode material for next-generation rechargeable battery technologies due to its high specific capacity (3862 mAh/g) and negative potential (−3.04 V vs standard hydrogen electrode, SHE).[4] Indeed, replacing graphite negative electrodes with metallic Li will enable the achievement of specific energy values at least double of those atteined in current LIBs, depending on the cathode chemistry (high-voltage lithium nickel manganese cobalt oxides $LiNi_xMn_yCo_zO_2$ (NMC) with $x \geq 0.8$,[5] sulfur,[6] or oxygen[7]). However, due to its high reactivity, Li metal is unstable towards commercial liquid electrolytes,[8] making the system prone to dendrite formation and, therefore, posing serious safety concerns and poor Coulombic efficiency.[9,10] Current half-cells (e.g. Li vs NMC-based cathode) contain an excess of Li (foils with a thickness of 20 μm are commonly used in batteries with a polymer electrolyte), which is necessary to allow their cycling when the plating/stripping process is not efficient. This is related to the irreversible loss of Li, known as "dead" lithium, as the consequence of inhomogeneous electrochemical reactions and mechanical strains.[11] Although the formation of dead Li cannot be avoided, the amount of Li metal used in battery cells must be minimized due to its high costs and low recyclability rate.[12] Therefore, the use of a positive electrode as the source of Li+ cations will enable to reach higher energy density when Li+ ions will plate onto a thin current collector during the first charge step ("anode-less" configuration), thereby reducing the amount of Li metal used in the cell.[13] Together with the formation of dead Li, other phenomena, such as dendrite formation,[14] corrosion,[15] volume expansion,[16] degradation of current collectors[17] and transition metal dissolution[18] prevent further development of Li metal batteries.

**ADVANCED
SCIENCE NEWS**

www.advancedsciencenews.com

**ADVANCED
MATERIALS
TECHNOLOGIES**

www.advmattechnol.de

Optical microscopy techniques are known to be intrinsically non-perturbing and information-rich methods. Therefore, great research efforts pushed towards their implementation in battery science to probe the formation and evolution mechanism of Li metal deposition. In agreement with Sano et al.,[19] Nishida et al.[20] have shown the plating of Li metal in ionic liquid electrolytes by using a three-electrode system without applying external pressure on Li metal. Steiger et al.[21] have observed the plating of Li metal needles on tungsten metal with 1M $LiPF_6$ in ethylene carbonate:dimethyl carbonate (1:1) electrolyte at low current density (2 $\mu A\ cm^{-2}$). Love et al.[22] have detected mushroom-like Li metal deposits in a temperature range from −20 to 20 °C. Chen et al.[23] have investigated the intercalation of Li^+ ions between graphite layers by using a three-electrodes cell, observing the formation of golden LiC_6 and subsequent Li metal plating. By using a similar setup, Sanchez et al.[24] have investigated Li plating on Li metal foil in a current density range between 0.25 and 2 mA cm^{-2}, showing that Li dendrites preferentially nucleate in correspondence with grain boundaries. Wood and co-workers[25] have been able to detect the propagation, detachment, and dissolution of Li metal dendrites in the electrolytes by testing different carbonate and ether-based solutions. Under *operando* conditions, Kazyak et al. [26] used a top-view setup to monitor the copper (Cu) current collector deformation due to Li metal plating, as a function of the applied force. Merryweather and co-workers[27] showed the ability of bright field microscopy methods to monitor Li deposition and diffusion, while a similar optical approach was applied by Cheng et al.[28] to obtain a side view of a Li metal electrode via Raman spectroscopy.[29,30] By using transmission electron microscopy (TEM), Xu et al.[31] were able to detect the solid electrolyte interface (SEI)[32] formation on the Cu anode. These methods clearly showed the potential of optical methods to unveil the internal processes of energy storage devices. However, the reported cell geometries lack in mimicking the real application parameters, such as internal cell pressure and electrolyte/areal loading ratios, which are commonly used in laboratory-scale batteries and industrial energy storage devices.[33]

To overcome this challenge, our group has developed an innovative optical approach that provides qualitative insights into the correlation between surface characteristics and dynamic nucleation of Li metal during cycling, when an anode-less coin cell setup was used. Herein and for the first time, we used *operando* optical microscopy to monitor the time-resolved Li metal plating with through-plane observations. To enable this, commercial coin cell casing has been customized with a specially designed indium tin oxide-polyethylene terephthalate (ITO-PET) substrate, which acts both as the conductive current collector and transparent optical window. Our results represent an important step towards understanding the Li metal deposition mechanism and possible secondary reactions involving the layer-by-layer growth of dead Li metal in anode-less configuration.[13] Interestingly, it was observed that dead Li islands own electronic conducting and ionic passivating nature. These findings were complemented by computer vision data analyses to evaluate the evolution of the dimensions of the Li deposits. In previous works it was not possible to observe Li metal plating directly: Kazyak et al.[26] could detect only the Cu foil deformation as a consequence of Li metal deposition. Therefore, in that case, the Cu foil must be lifted to form an island that can be visualized but, unfortunately, early

stages or small changes in Li plating/stripping stay therefore undetected. Furthermore, physicochemical characterization methods were used to elucidate the properties of the SEI deposited on the ITO-PET window. Straightforward access and visualization to these processes are pivotal to putting in place strategies to mitigate and, eventually, overcome inhomogeneous and irreversible Li plating.

2. Results and Discussion

The schematics in **Figure 1** show the newly developed positive casing of a CR2032 coin cell (Figure 1a) and the *operando* optical microscopy set-up (Figure 1b) used in this work, respectively. A Cu tab was used to ensure the electron flow between the positive casing and ITO window due to the electron-insulating nature of the PET layer. The ITO-PET transparent window allows the optical recordings of the changes that occurred to the ITO surface, which are synchronized with the electrochemical response of the as-assembled anode-less cells during slow (C/40) and fast (2C) cycling. Figure S1 (Supporting Information) shows the bare ITO-PET window surface before cycling. In literature ITO shows a lithophilic behavior[34]: during the charging process, ITO layer undergoes an alloying process that results in the formation of $Li_x In$, $Li_x Sn$, and $Li_2 O$, as reported by Yan et al.[35]

Li plating and stripping were first performed using C/40 current density, as shown in **Figure 2** (see Video S1, Supporting Information for more details). Although the ITO layer is reduced,[36] the window conductivity is probably ensured by the formation of polyradical anions at the ITO-PET interface at potentials below 1.2 V vs Li^+/Li.[37] A darkening of the focal plane is observed starting from 19 min of charging, which corresponds to a potential of 2.77 V vs Li^+/Li. This might be related to the initial decomposition of the electrolyte solution at the ITO surface to form a rough layer, resulting in the reduction of the reflectance of the window.[23] After circa 28 min (2.89 V vs Li^+/Li), blue horizontal lines appear on the surface of the ITO window upon Li plating (Figure 2-panel 1). ITO coated on polymer supports can encounter channel cracking and interfacial delamination,[38] as shown by atomic force microscopy (AFM) imaging in Figure S2 (Supporting Information). These aligned defects can act as preferential spots for the initial plating of Li metal, resulting in blue-colored lines. Upon Li plating, color transitions from blue to red and, further, to golden were observed after circa 37 min (3.04 V vs Li^+/Li) and 44 min (3.13 V vs Li^+/Li), respectively. The color transition of the ITO window can possibly be related to the change of oxidation state of the Sn and In transition metal cation during the reduction reaction (alloying reaction with Li^+ cations).[35,39] Together with the color transition, a lightening of the ITO-PET substrate is detected starting at $t = 62$ min (3.29 V vs Li^+/Li). This phenomenon is associated with the parasitic decomposition reactions of the electrolyte solution when in contact with highly reactive Li metal to form a non-uniform and passivating SEI layer.[40] The color transition of the substrate is, therefore, ascribed to the change of its superficial characteristics, as already observed after the first minutes of cycling.[23] Upon charge, Li metal initially nucleates at the intersection of the horizontal and oblique defect lines ($t = 70$ min, 3.44 V vs Li^+/Li). Starting from these "hot spots", preferential pathways for Li deposition are observed along the oblique defect lines, resulting in the formation

**ADVANCED
SCIENCE NEWS**

www.advancedsciencenews.com

**ADVANCED
MATERIALS
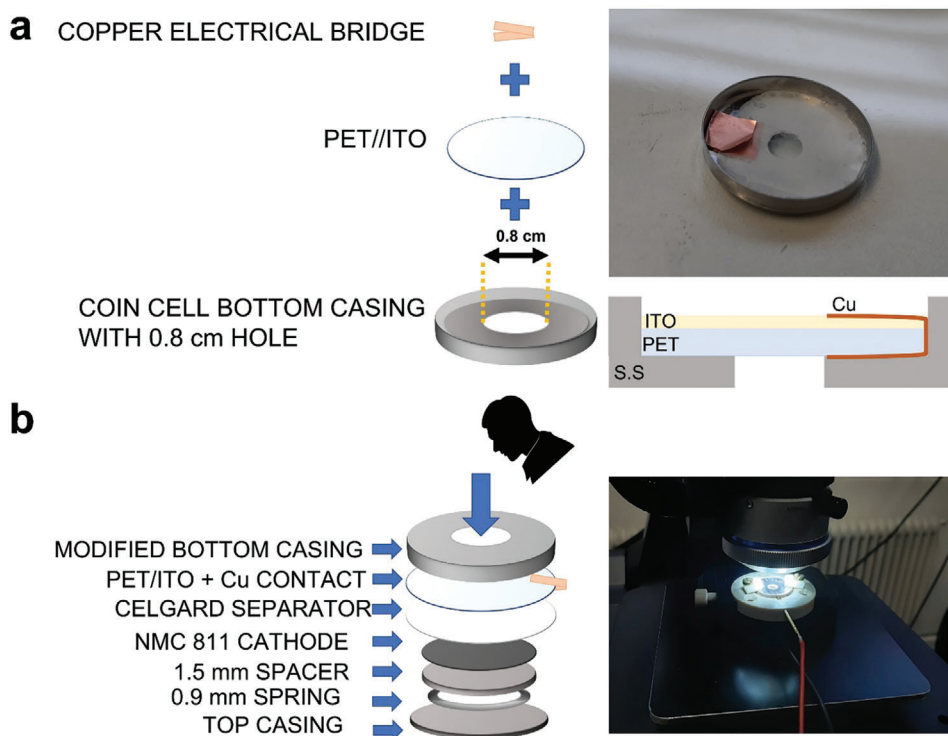TECHNOLOGIES**

www.advmattechnol.de

Figure 1. Schematics and images of the a) modified bottom casing with transparent ITO-PET window and b) *operando* cycling setup.

of petal-like structures in the focal plane ($t = 113.5$ min, 3.62 V vs Li$^+$/Li), as shown in Figure 2-panel 2. It is important to note that the nucleation and growth of Li are intimately connected with the heterogeneous nature of the structure and composition of the surface. Dislocations, grain boundaries, defects, surface pre-treatments (mechanical/chemical polishing), electrolyte, and SEI compositions[41] influence the dynamic nucleation process causing differences in activation energies for dendrite formation and nucleation density.[42,43] As a control analysis, the dU/dt curve was calculated and it was observed that all the above phenomena result in peak maxima as they are correlated to the changes in slope in the voltage curve (Figure S3, Supporting Information). Together with the preferential deposition in petal-like structures at the bottom of the window, Li plates with spongy morphology (mossy Li) inside these structures in the top part, as shown in Figure S4 (Supporting Information). The in-plane spatial heterogeneity of Li deposition is related to the concentration saturation of the surface as a function of time. In fact, Li deposits with different rates lead to the saturation of some areas, changes in reaction pathways, and nucleation of Li in other spots.[23] Therefore, proceeding with cycling, the deposition of mossy lithium is observed in different areas of the focal plane, while, in the areas already populated with mossy Li, fresh Li is plated. The continuous deposition of Li ($t = 325$ min, 3.64 V vs Li$^+$/Li) results in the nucleation of dendritic Li with thin needles morphology (Figure 2-panel 3)[21] over the mossy one. This is because lithium metal dendrites prefer to grow from pre-existing Li structures rather than forming new nuclei.[25] These dendrites continue to grow during plating (bottom-up view in the plan-view perspective) and spread further on the surface leading to larger structures, as

shown in Figure S5 (Supporting Information). It was noted that the dendritic Li (mossy and needle morphologies) are golden colored although similar optical microscopy investigations show the plating of black metal Li deposits.[23,25,20] It is believed that the use of ITO-PET substrate may play a significant role in the reflectance of the surface and, therefore, on the shades of the deposited species. However, the further understanding of this optical phenomenon is beyond the scope of this work. The plating and accumulation of needle-shaped Li dendrites characterize the charging step, as shown in Figure 2-panel 4. By contrast, during the constant voltage and discharge steps, the dissolution of the needle-shaped dendrites and the formation of dead Li[44] were detected. Li dendrites shrink but do not dissolve completely as observed by comparing panels 5–6 in Figure 2 (see Video S1, Supporting Information for more details). It was noted that needle-shaped Li dendrites are prone to dissolve from the interface with the ITO-PET substrate starting from $t = 50.70$ h (4.2 V vs Li$^+$/Li), which corresponds to the beginning of the constant voltage step. The stripping of Li$^+$ ions from the dendritic Li continues upon discharge, leading to the segregation of Li particles from the electric conductive layer to form dead Li.[45] The detachment of Li metal is completed at $t \approx 110$ h (3.48 V vs Li$^+$/Li) when a darkening of the focal plane and dead Li deposits is detected.[25] The color change is ascribed to the modification of the surface properties of the SEI layer (e.g. roughness), which is deposited on the surface of mechanically detached Li (contraction of volume).[23] These phenomena correspond to two peaks visible in the dU/dt curve (Figure S6, Supporting Information).

To confirm these observations, the evolution of the Li surface was analyzed during the second and third charge-discharge
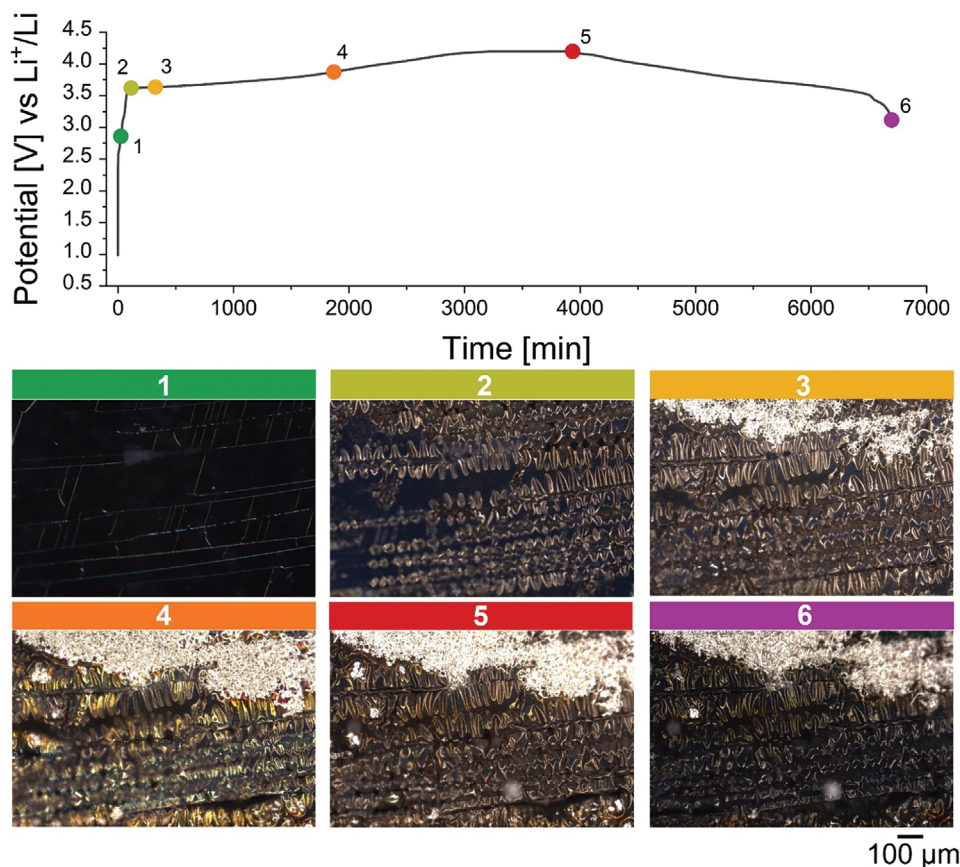
2301902 (3 of 10)

**ADVANCED
SCIENCE NEWS**

www.advancedsciencenews.com

**ADVANCED
MATERIALS
TECHNOLOGIES**

www.advmattechnol.de

Figure 2. Evolution of Li-plating/stripping during the first charge and discharge cycle at a low C-rate.

cycles. **Figure 3a** provides the stepwise visualization of the dendrite's growth after the first cycle and the behavior of dead Li in the following two cycles. Dendrites grow in a silver wires-shaped fashion: after the second and third discharge steps, it was possible to monitor the evolution of dead Li from dendrites that evolved during the plating processes. The growth of dead Li islands could be monitored for both cycles. During the second charge (Figure S7, Supporting Information), Li metal starts to nucleate along the petal-like structures that cover regions not occupied by previously deposited dead lithium (t = 112.15 h, 3.61 V vs Li⁺/Li). In parallel, mossy Li is also formed upon Li deposition and is localized within the petal-liked structures. Successively, the dendrite growth continues as needle-shaped structures (t = 112.35 h, 3.61 V vs Li⁺/Li). As described for the first discharge step, an intergrowth of dead Li was observed at the end of the second discharge (t = 193 h, 3.00 V vs Li⁺/Li), leading to a denser and more tortuous interphase. Interestingly, it was noted that dead Li deposits over previous layers of dead Li, which nucleated after the first cycle. This possibly suggests that the dead Li interphase owns an electronically conductive nature, while not being permeable to the diffusion of Li⁺ ions. In fact, no dead Li dissolution was observed, whereas an enlargement of the detached Li metal areas was detected during the third charge-discharge cycle (Figure S8, Supporting Information). Thus, the accumulation of the unreacted Li metal leads to an irreversible capacity loss of the anode-less cell, showing a decrease of the specific capac-

ity of 25.8% from the first (298.83 mAh g⁻¹) to the third (221.74 mAh g⁻¹) cycle. Although SEI deposition also accounted for the cell inefficiency, the formation of dead Li mainly contributes to capacity decay when carbonate electrolytes are used.[31] In order to analyze the impact of the growth of dead Li clusters on the cycling behavior, we identified and compared the number and mean radii of circular blobs in selected areas of the micrographs after Li⁺ ions stripping (Figure 3b). These clusters are defined as regions of the image with different attributes (e.g. brightness, contrast, or pixel intensity values) compared to the background. The applied approach to detection, classification, and quantification of such clusters grounds on the Laplacian of Gaussian (LoG) algorithm.[46] First, the input image $I(x,y)$ with adjusted values of contrast and brightness is convolved by a Gaussian kernel (Equation 1):

$$g(x, y, t) = \frac{1}{2\pi t}e^{-\frac{x^2+y^2}{2t}} \tag{1}$$

The Laplacian operator (L) is then computed (Equation 2) with t scale:

$$\nabla^2 L = L_{xx} + L_{yy} \tag{2}$$

Blobs with radii $r^2 = 2t$ can be computed for the plan-view imagining of the Li deposits. The inspection of the

**ADVANCED
SCIENCE NEWS**

www.advancedsciencenews.com

**ADVANCED
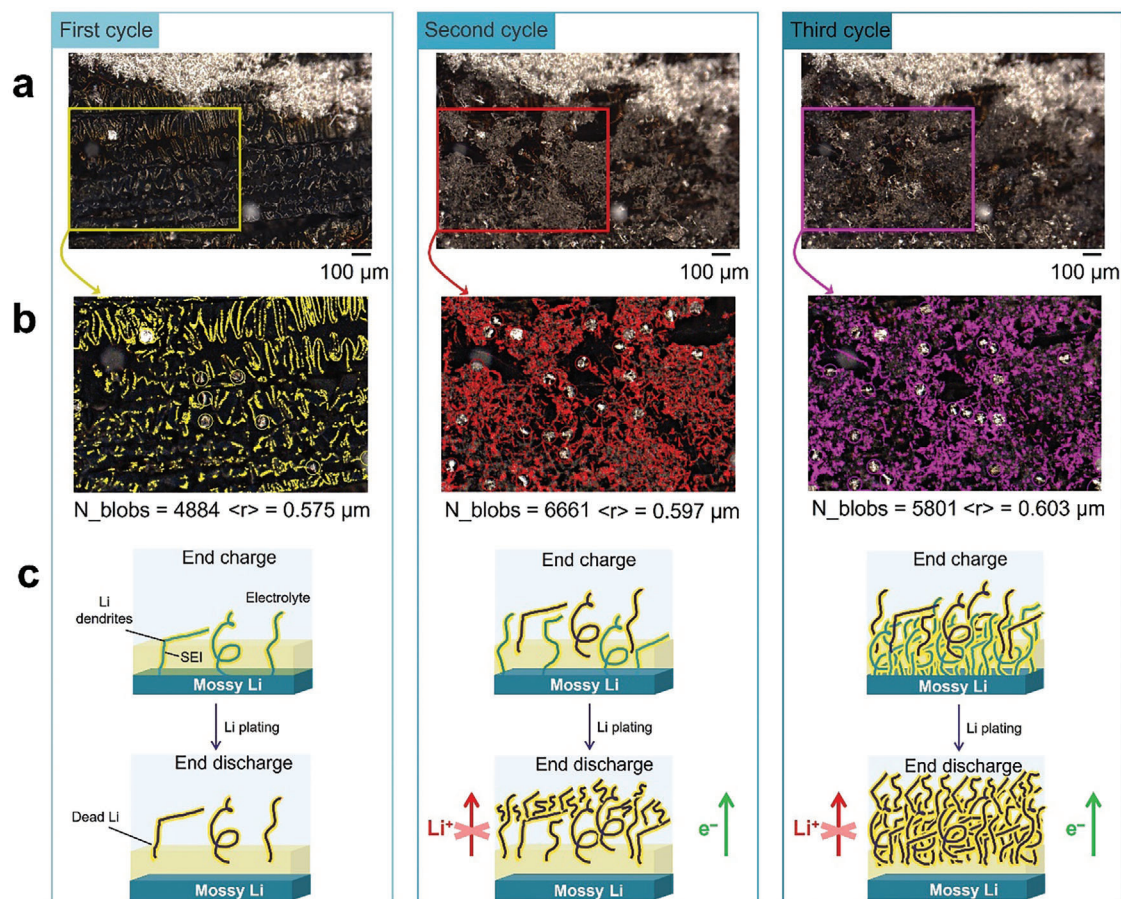MATERIALS
TECHNOLOGIES**

www.advmattechnol.de

Figure 3. a) Continuous deposition of lithium after the first, second, and third discharge cycles showing the formation and growth of dead lithium. b) Image analyses and blob detection on selected Regions of Interest to identify and quantify dead Li clusters formed after the first (yellow circles), second (red circles), and third (purple circles) cycle. c) Schematics representing the mechanism of Li dendrite nucleation (left), growth (middle), and dead Li formation (right) in the first, second, and third discharge cycles, respectively.

high-resolution digital images revealed the presence of blobs which are related to the dead Li clusters, as the result of cycling. It is important to underline that the number of blobs and their mean radii are proportionally correlated after the first and the second discharge cycles, confirming that Li metal preferentially plates over previously deposited Li grains (layer-by-layer growth). The mean radii of the clusters increase also upon the last stripping step, although the number of clusters decreases. This aspect might be correlated to the coalescence of dead Li islands across the selected area (Figure 3c).

Cells were also cycled at a higher C-rate (2C) to evaluate the differences in the dynamic deposition and plating of Li metal since it is known that Li dendrite growth is greatly affected by current density (**Figure 4**; Video S2, Supporting Information).[47] Defects run along the surface defects of the ITO-PET window, as observed in the cell cycle at a lower current. However, it was noticed that Li does not deposit in these defects upon the first stage of the charging step. On the other hand, after 2.47 min (4.16 V vs Li+/Li) a darkening of the focal plane and the beginning of Li deposition were observed. The color of the background is related to the deposition of an SEI layer that changes the reflectance prop-

erties of the ITO-PET window.[23] Differently to the cell cycle at a lower C-rate, Li metal deposits grain-by-grain resulting in two larger circular elements. Upon charge, the areas at the boundaries of these elements shade from brown to blue, changing to red and golden in the second stage. In addition, the color transition is not homogenous on all the focal planes. Following the classical nucleation theory, it is known that the current density is correlated to the deposition overpotential and, therefore, influences the plating of Li. Increasing the current density, a higher nucleation density and, hence, higher heterogeneity of the Li deposits were observed.[48] At $t = 3$ min (4.16 V vs Li+/Li), the color of the grain, which forms the bigger circular structure, changes from grey to blue. Furthermore, the defects shade from white to golden. These color changes can possibly be related to the ITO surface reduction, as alloying reactions take place between the transition metal cations (Sn and In) and Li.[35] Petal-like structures form at the boundaries of the line-shaped defects and the rounded structure after 3.13 min (4.15 V vs Li+/Li). Golden areas populate the focal area as mossy Li deposits start to nucleate. These structures interconnect to each other and grow upon Li deposition ($t = 3.6$ min, 4.14 V vs Li+/Li), as shown in Figure 4b-panel 1. Computer vision data calculation shows that the size
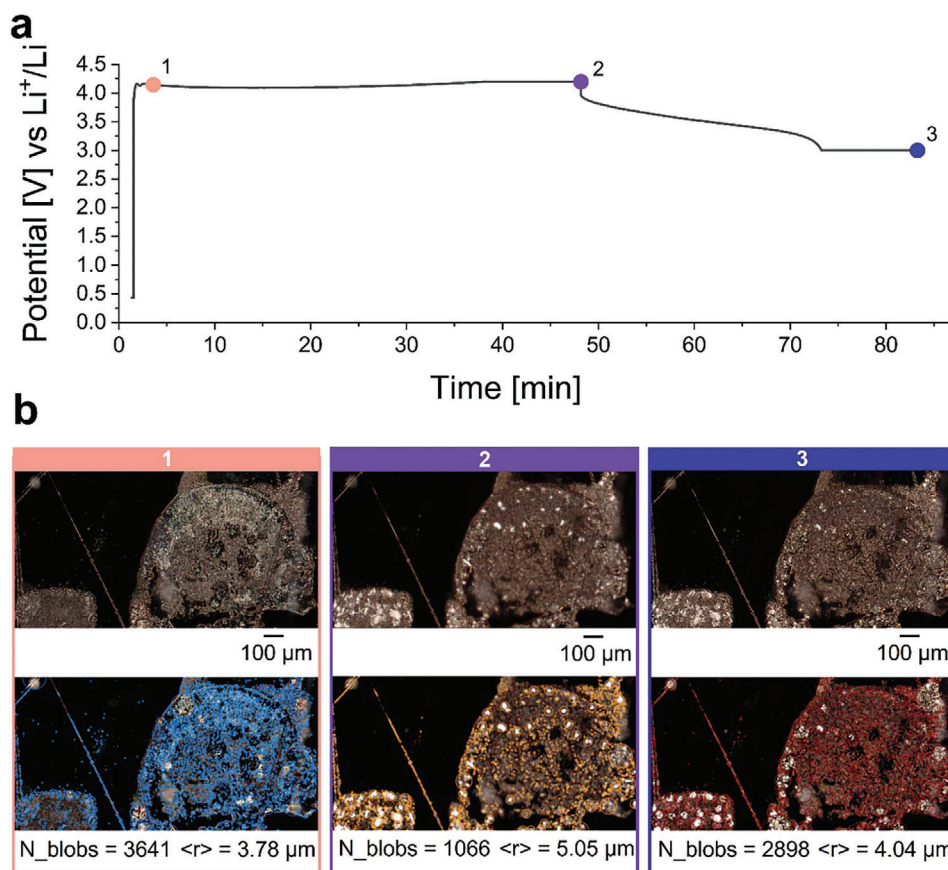
Figure 4. Charge/discharge curve at high C-rate, optical microscope images, image analyses and blob detection on selected Regions of Interest.

of these Li clusters is ≈ 0.582 µm. Moreover, partial dissolution of Li was also detected as local oxidation occurs in areas with higher state of charge (SOC), as already reported for lithiation of graphite electrodes.[49] Needle-like dendrites grow and enlarge to form bright spots with sizes up to 0.776 µm starting from $t = 6.08$ min (4.14 V vs Li$^+$/Li) and, also, throughout the constant voltage step (Figure 4b-panel 2). Li stripping was detected upon discharge and during the subsequent constant voltage step (Figure 4b-panel 3), resulting in the shrinkage of the golden deposits and the formation of hollow dead Li structures (Figure S9, Supporting Information). As higher nucleation density is expected at the grain boundaries, these hollow dead Li deposits might be related to the preferential dissolution (lower activation energy) of Li, which was plated on the surface grains. As already observed for the cell cycled at low C-rate, the presence of peaks in the dU/dt curves confirmed the plating of Li metal and the formation of mossy Li and, at the end of discharge, hollow dead Li structures (Figure S10, Supporting Information). However, the plot resolution is not optimal due to the high acquisition rate during cycling.

To better understand the influence of the current density on the plating-stripping process, the average size of the Li agglomerates was measured at different SOCs of the anode-less cell during the first charge-discharge cycle in both C-rate regimes (**Figure 5**). The detailed analysis of each collected point is reported Figures S11–S12 (Supporting Information). Considering the low C-rate
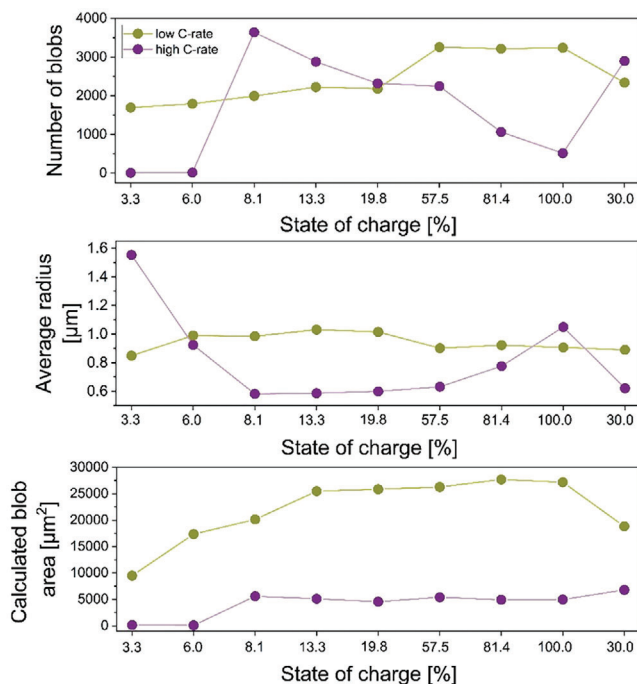

Figure 5. Number of blobs, average radius, and calculated blob area for anode-less cells cycled at low and high C-rates after the first cycle.

**ADVANCED
SCIENCE NEWS**

www.advancedsciencenews.com

**ADVANCED
MATERIALS
TECHNOLOGIES**

www.advmattechnol.de

Table 1. Infrared frequency assignment for the main band of ITO-PET windows cycled at low (C/40) and high (2C) C-rates.

Species	Vibration mode	Experimental band position [cm⁻¹]		Reference
		Low C-rate cell	High C-rate cell	
P—F containing moieties	symmetric stretching	876	876	Pekarek et al.[53]
F—P—F containing moieties	scissoring bending	558	557	Pekarek et al.[53] Abramowitz et al.[54]
Li—F in LiF	symmetric stretching	779	775	Abramowitz et al.[54]
		501		
C(=O)—O for species in the solvent mixture	symmetric stretching	1264	1264	Grugeon et al.[56]
C—O in Li₂CO₃	symmetric stretching	1484	1484	Grugeon et al.[56]
		1411	1412	
C—O in Li₂C₂O₄	symmetric stretching	1404	1405	Grugeon et al.[56]
		1380	1380	
HCO₂Li				
C=O in Li₂C₂O₄	symmetric stretching	–	1621	Grugeon et al.[56]
HCO₂Li				
C=O for species in the solvent mixture	symmetric stretching	1778	1777	Pekarek et al.[53]
		1769	1769	Shi et al.[57]
				Grugeon et al.[56]
C≡C in Li₂C₂	stretching	2131	2134	Ssenyange et al[65]
O—H in LiOH	symmetric stretching	–	3671	Weber et al.[59]

cell (green line), the number of blobs and their average areas increase upon charge. As previously observed in Figure 3, this indicates the tendency of Li to plate over already deposited Li, thereby enlarging these metallic islands up to a mean radius of 0.89 µm after the discharge step. On the other hand, the dimensions of the Li deposits slowly increased upon plating when the anodeless cell was cycled at a higher C-rate (purple line), although a co-alescence phenomenon occurred due to the formation of lithium agglomerates (Figure 4). At high current, Li deposits do not have sufficient time to electrochemically dissolve. Therefore, the area of such blobs remains constant and/or increases by 5-10% factor per cycle.

In view of these results, it is possible to conclude that i) Li dendrites at low C-rate are bigger than those formed upon cycling at higher C-rate and ii) the stripping step is poorly reversible at low currents.

To confirm the conductive properties of the SEI layers, morphological and compositional investigations were performed on the ITO-PET windows cycled at low and high C-rates. In Figure S13 (Supporting Information), X-ray diffraction patterns show the peaks of Li (1 1 0) and Li₂O for both samples, proving the deposition of lithium on the ITO-PET windows (negative electrode) during cycling, as already reported in literature.[50,51] Similarly to the work of Kaboli et al.,[52] LiF, LiOH, and small diffraction peaks of Li₂CO₃ indicate the formation of a SEI layer. The intensities of these peaks are generally higher for low C-rate indicating a higher crystallinity of the precipitated phases. This phase identification is supported by infrared spectroscopic characterization (Figure S14, Supporting Information). The fingerprint and functional group absorption regions of both spectra are comparable, even though the peaks are better defined and show higher intensities in the sample cycled at a high C-rate, sug-

gesting the formation of a thicker and denser SEI layer (Figure S15, Supporting Information). As the same electrolyte is used in the electrochemical cells, the SEI layers are both composed of similar inorganic and organic species with the characteristic bands reported in **Table 1**. Fluorinated moieties were detected in both samples, in particular, the vibration of P—F bond and Li—F were assigned in the far infrared region.[53,54] The characteristic vibrational bands of carboxylate and alkyl carbonate bonds were detected for the C(=O)—O symmetric stretching (1264 cm⁻¹),[55] C—O symmetric stretching of Li₂CO₃, lithium oxalate (Li₂C₂O₄) and lithium formate (HCO₂Li).[56] The appearance of a broad peak at 1621 cm⁻¹ in the high C-rate spectrum was also observed (marked with an asterisk) and potentially assigned to the symmetric stretching of C=O bond in Li₂C₂O₄ and HCO₂Li.[56] The spectral region 1780-1760 cm⁻¹ is populated by bands assigned to the symmetric stretching of the C=O bond, which characterize the species in the solvent mixture.[56,57] Furthermore, the presence of Li₂C₂ was also observed in the infrared spectra of both samples.[58] In fact, a small band of the carbon triple bond stretching occurs at 2131 and 2134 cm⁻¹ for the low C-rate and high C-rate samples, respectively. Moreover, the hydroxyl symmetric stretching band of LiOH[59] was also observed in the high C-rate spectrum at 3671 cm⁻¹. Scanning electron microscopy images in Figure S16 (Supporting Information) of the cycled ITO-PET window at high C-rate shows the presence of cracks as a result of the mechanical stress produced by the dendrite propagation, as reported by McConohy et al..[60] These morphological and chemical analyses show that a SEI layer with cationic-insulating properties possibly encapsulates the formed dead Li. In fact, the main detected components (e.g. LiF, Li₂O, and Li₂CO₃)[61–64] show ionic conductivity values ranging between 10^{-12} and 10^{-8} S cm⁻¹.

**ADVANCED
SCIENCE NEWS**

www.advancedsciencenews.com

**ADVANCED
MATERIALS
TECHNOLOGIES**

www.advmattechnol.de

3. Conclusion

This work shows the fabrication of a novel coin cell set-up equipped with an ITO-PET transparent window that allows to monitor the plan-view growth of lithium metal under practical electrochemical conditions, providing significant insights into its plating/stripping mechanism. Lithium metal nucleates with a mossy morphology and, further, agglomerates over this layer to form needle dendrites and, finally, dead Li deposits, when low C-rate currents were applied. At high C-rate currents, it was possible to detect the instantaneous formation of a thick SEI layer and hollow dead Li structures. By analyzing the agglomerate size, it was calculated that the deposits in the high C-rate sample have a smaller average area than those observed in the low C-rate cell. As an important novelty, it was detected that the dead lithium deposits grow layer-by-layer during cycling, showing its poor reversibility. During cycling, the accumulated dead Li gradually evolves in a thick layer showing a more tortuous pathway for Li$^+$ ions as proposed by Chen et al.[66] The fundamental knowledge attained in this work can be leveraged to design electrode materials and electrolyte solutions which will enable to reduction of voltage inhomogeneities and tune the chemical composition at their interphase. It is also believed that this new cell set-up can be implemented in other battery chemistries such as quasi-solid (gel-polymer) and solid-state (polymer, ceramic, or hybrids) anode-less Li metal batteries to elucidate the nucleation behavior of Li in real-time conditions. Furthermore, considering the reactivity of ITO, different metals could be sputtered on the ITO-PET window to reduce side reactions and tune its lithiophilicity.[67] This would aid in gaining insights into the effect of the electrode surface chemistry on the deposition of Li metal in its different morphologies. The future use of confocal methods may also allow of following the three-dimensional evolution of the Li plated structures, to expand the understanding gained in this work.

4. Experimental Section

Window Preparation: The positive pole of a CR2032 coin cell was modified by boring a hole of 8 mm diameter, then applying a window of ITO-PET (Sigma Aldrich) that was sealed by using Torr Seal glues (Agilent). The electrical contact between the conductive ITO and coin cell casing was created by using a copper (MTI) strip. Subsequently, the positive pole modified with the ITO window was dried at room temperature for 24 h before being used as the bottom casing. A further Cu ring with 19 mm external diameter and 9 mm internal diameter was used to analyze the sample at high C-rates (2C) in order to facilitate the electrical conduction.

Electrode Preparation and Battery Assembly: NMC622 (Ronbay product S85EL) working electrodes were prepared by a slurry deposition method. Prior to the slurry preparation, polyvinylidene fluoride (Solef PVDF, Solvay SA) was dissolved in 1-methyl-2-pyrrolidinone (Sigma Aldrich, anhydrous, 99.5% purity) to form an 8 wt% binder solution. Successively, NMC622 and carbon black (SuperC65, C-NERGY) were added to the binder solution and a few grams of additional solvent were added to reach a solid content of 65 wt%. The mixture was mixed for 5 min at 3000 rpm in a 250 mL vessel with a dissolver blade (DISPERMAT CV3-PLUS, VMAGETZ-MANN GMBH, Reichsdorf, Germany). The NMC622:carbon:binder ratio was set to 93:3:4. The roll-to-roll coating process was conducted via doctor blade coating method (SC 30, COATEMA Coating Machinery GmbH, Dormagen, Germany) with a gap width of 310 μm using a 22 μm thick aluminum foil (Norsk Hydro ASA, Oslo, Norway) as the current collector. Drying was ensured by the combination of three sequential drying phases

at 85, 105, and 95 °C and a line speed of 0.5 m min^{-1}. After the drying step, several circular electrodes were cut with a diameter of 15 mm and dried at 120 °C for 12 h under vacuum before being introduced directly into an Ar-filled glove box (< 0.1 ppm H$_2$O and O$_2$). The electrode loading was 5 mAh cm^{-2}. Modified CR2032 coin cells (Figure 1a) were assembled using the as-prepared electrode as the working electrode, PET-ITO window as the counter electrode, a membrane separator (Celgard 2500) and 150 μL of 1 M LiPF$_6$ in ethylene carbonate:ethyl methyl carbonate = 3:7 w/w with 2 wt% vinylene carbonate (Soulbrain, PuriEl Battery Electrolyte) electrolyte solution.

Operando Optical Microscopy: The modified coin cells were used to perform *operando* optical microscopy experiments under galvanostatic electrochemical conditions (Figure 1b). A BioLogic SP300 potentiostat was used for galvanostatic cycling. The coin cells were cycled in the potential range between 3.0 and 4.2 V vs Li$^+$/Li with a current of 4.32 mA, which is defined as 1C, at C/40 and 2C rates. The cells were allowed to rest for 1 h after both the charge and discharge steps. Optical microscope images were acquired using a Keyence VHX-7000 digital microscope recording at a rate of 20 s per frame. Due to the interesting features detected during imaging, video footage for the initial 2 h was also recorded (see supporting material). Focus variation was applied throughout the cycling to maintain the deposited, mossy, and dendritic Li surfaces in focus. Frames and videos were recorded using a 100× objective. After cycling, the cells were disassembled in an Ar-filled glove box in order to collect the ITO electrodes and perform further *post-mortem* characterization.

Computer Vision Data Analysis: Snapshots from video acquisition were extracted to obtain the digital images for blob detection, classification, and quantification. These images were processed using an unsharp mask and converted to grayscale images with the gamma curve corrected. Finally, a LoG blob detection was performed by applying the same thresholds (minimum and maximum Gaussian kernel size values of 1 and 25 pixels, respectively) to all images to obtain internally consistent data set values of the detected blobs and blob area extension.

X-Rays Diffraction: Structural characterization of the cycled ITO electrodes was carried out by powder X-ray diffraction (XRD) using a Malvern Panalytical X'Pert Pro diffractometer with Cu-Kα radiation (λ = 1.5418 Å) in flat plate Bragg-Brentano geometry. The XRD measurements were performed in the 2θ range from 10° to 120°, with a step size of 0.0334° and an effective count time of 400 s per step. To prevent exposure to air, the electrodes were fixed onto a silicon mono-crystal substrate in an airtight half-dome equipped sample holder (Bruker) inside the Ar-filled glove box and then transferred to the diffractometer for X-ray measurements.

Imaging: To evaluate the morphology of the deposited Li species, scanning electron microscopy (SEM) images were taken on a Carl Zeiss Supra 40 microscope equipped with Everhart–Thornley (ETD) and Through-Lens (TLD) detectors, using a primary electron-beam energy of 2 keV. The elemental mapping was performed by energy dispersive X-ray spectroscopy (EDS) using an Octane Elect detector (EDX, EDAX Inc., Mahwah, NJ, USA) and an electron-beam energy of 20 keV. The ITO electrodes were fixed onto an SEM sample holder in a glovebox and transferred to the SEM in an air-tight vessel. The maximum contact time of the electrodes with air during transfer to the SEM chamber was 3-5 s on average. The surface topography of the ITO-PET window was measured by atomic force microscopy (AFM) in the tapping mode using a Molecular Imaging, PicoPlus.

Fourier Transform Infrared Spectroscopy: Compositional studies on the SEI layers formed upon cycling were performed by *post-mortem* Fourier transform infrared (FTIR) spectroscopy. These measurements were carried out inside an Ar-filled glove box using a PerkinElmer Spectrum Two spectrometer with the attenuated total reflectance (ATR) technique. The infrared spectrum was collected in the 4000-450 cm^{-1} range after 256 scans at 4 cm^{-1} resolution on the electrodes.

Supporting Information

Supporting Information is available from the Wiley Online Library or from the author.

Acknowledgements

Conflict of Interest

The authors declare no conflict of interest.

Data Availability Statement

The data that support the findings of this study are available on request from the corresponding author. The data are not publicly available due to privacy or ethical restrictions.

Keywords

[1] M. Armand, J. M. Tarascon, *Nature* **2008**, *451*, 652.

[2] M. S. Whittingham, *MRS Bull.* **2008**, *33*, 411.

[3] T. Kim, W. Song, D. Y. Son, L. K. Ono, Y. Qi, *J. Mater. Chem. A Mater.* **2019**, *7*, 2942.

[4] W. Xu, J. Wang, F. Ding, X. Chen, E. Nasybulin, Y. Zhang, J.-G. Zhang, *Energy Environ. Sci.* **2014**, *7*, 513.

[5] T. Koç, M. Hallot, E. Quemin, B. Hennequart, R. Dugas, A. M. Abakumov, C. Lethien, J.-M. Tarascon, *ACS Energy Lett* **2022**, *7*, 2979.

[6] S. Bai, X. Liu, K. Zhu, S. Wu, H. Zhou, *Nat. Energy* **2016**, *1*, 16094.

[7] T. Zhang, H. Zhou, *Angew. Chem.* **2012**, *124*, 11224.

[8] A. Mauger, C. M. Julien, A. Paolella, M. Armand, K. Zaghib, *Materials Science and Engineering R: Reports* **2018**, *134*, 1.

[9] R. Khurana, J. L. Schaefer, L. A. Archer, *J. Am. Chem. Soc.* **2014**, *136*, 7395.

[10] R. Xu, X. Q. Zhang, X. B. Cheng, H. J. Peng, C. Z. Zhao, C. Yan, J. Q. Huang, *Adv. Funct. Mater.* **2018**, *28*, 1705838.

[11] A. Kushima, K. P. So, C. Su, P. Bai, N. Kuriyama, T. Maebashi, Y. Fujiwara, M. Z. Bazant, J. Li, *Nano Energy* **2017**, *32*, 271.

[12] Y. Guo, H. Li, T. Zhai, *Advanced Materials* **2017**, *1700007*, 1.

[13] P. Molaiyan, M. Abdollahifar, B. Boz, A. Beutl, M. Krammer, N. Zhang, A. Tron, M. Romio, M. Ricci, R. Adelung, A. Kwade, U. Lassi, A. Paolella, *Adv. Funct. Mater.* **2023**, *34*, 2311301.

[14] M. Dollé, L. Sannier, B. Beaudoin, M. Trentin, J. M. Tarascon, *Electrochem. Solid-State Lett.* **2002**, *5*, A286.

[15] S. Chen, X. Yang, J. Zhang, J. Ma, Y. Meng, K. Tao, F. Li, J. Geng, *Electrochim. Acta* **2021**, *368*, 137626.

[16] Q. Wang, B. Liu, Y. Shen, J. Wu, Z. Zhao, C. Zhong, W. Hu, *Adv. Sci.* **2021**, *8*, 2101111.

[17] L. Guo, D. B. Thornton, M. A. Koronfel, I. E. L. Stephens, M. P. Ryan, *J. Phys. Energy* **2021**, *3*, 032015.

[18] D. Huang, C. Engtrakul, S. Nanayakkara, D. W. Mulder, S.-D. Han, M. Zhou, H. Luo, R. C. Tenent, *ACS Appl. Mater. Interfaces* **2021**, *13*, 11930.

[19] H. Sano, H. Sakaebe, H. Matsumoto, *J. Power Sources* **2011**, *196*, 6663.

[20] T. Nishida, K. Nishikawa, M. Rosso, Y. Fukunaka, *Electrochim. Acta* **2013**, *100*, 333.

[21] J. Steiger, D. Kramer, R. Mönig, *Electrochim. Acta* **2014**, *136*, 529.

[22] C. T. Love, O. A. Baturina, K. E. Swider-Lyons, *ECS Electrochem. Lett.* **2014**, *4*, A24.

[23] Y. Chen, K.-H. Chen, A. J. Sanchez, E. Kazyak, V. Goel, Y. Gorlin, J. Christensen, K. Thornton, N. P. Dasgupta, *J. Mater. Chem. A Mater.* **2021**, *9*, 23522.

[24] A. J. Sanchez, E. Kazyak, Y. Chen, K.-H. Chen, E. R. Pattison, N. P. Dasgupta, *ACS Energy Lett.* **2020**, *5*, 994 .

[25] K. N. Wood, E. Kazyak, A. F. Chadwick, K.-H. Chen, J.-G. Zhang, K. Thornton, N. P. Dasgupta, *ACS Cent. Sci.* **2016**, *2*, 790.

[26] E. Kazyak, M. J. Wang, K. Lee, S. Yadavalli, A. J. Sanchez, M. D. Thouless, J. Sakamoto, N. P. Dasgupta, *Matter* **2022**, *5*, 3912.

[27] A. J. Merryweather, C. Schnedermann, Q. Jacquet, C. P. Grey, A. Rao, *Nature* **2021**, *594*, 522.

[28] Q. Cheng, L. Wei, Z. Liu, N. Ni, Z. Sang, B. Zhu, W. Xu, M. Chen, Y. Miao, L.-Q. Chen, W. Min, Y. Yang, *Nat. Commun.* **2018**, *9*, 2492.

[29] M. Rosso, C. Brissot, A. Teyssot, M. Dollé, L. Sannier, J.-M. Tarascon, R. Bouchet, S. Lascaud, *Electrochim. Acta* **2006**, *51*, 5334 .

[30] I. Rey, J. C. Lassègues, P. Baudry, H. Majastre, *Electrochim. Acta* **1998**, *43*, 1539.

[31] Y. Xu, H. Jia, P. Gao, D. E. Galvez-Aranda, S. P. Beltran, X. Cao, P. M. L. Le, J. Liu, M. H. Engelhard, S. Li, G. Ren, J. M. Seminario, P. B. Balbuena, J.-G. Zhang, W. Xu, C. Wang, *Nat. Energy* **2023**, *8*, 1345.

[32] M. Golozar, A. Paolella, H. Demers, S. Bessette, M. Lagacé, P. Bouchard, A. Guerfi, R. Gauvin, K. Zaghib, *Commun Chem* **2019**, *2*, 131.

[33] E. Miele, W. M. Dose, I. Manyakin, M. H. Frosz, Z. Ruff, M. F. L. De Volder, C. P. Grey, J. J. Baumberg, T. G. Euser, *Nat. Commun.* **2022**, *13*, 1651.

[34] Y. Jung, S. Park, J. K. Kim, M. Kim, B. Kang, *Adv. Funct. Mater.* **2022**, *32*, 2109759.

[35] X. Yan, F. Ye, Y. Zhang, L. Lin, B. Sa, F. Liu, J. Li, L. Wang, J. Lin, Q. Xie, D.-L. Peng, *Chem. Eng. J.* **2022**, *440*, 135827.

[36] L. Liu, S. Yellinek, I. Valdinger, A. Donval, D. Mandler, *Electrochim. Acta* **2015**, *176*, 1374.

[37] D. E. Nikles, M. S Farahat, *Macromol. Mater. Eng.* **2005**, *290*, 13.

[38] S. Ziaei, Q. Wu, J. Fitch, M. Elbadry, M. A. Zikry, *Exp Mech* **2019**, *59*, 703.

[39] Z. Ma, Z. Li, K. Liu, C. Ye, V. J. Sorger, *Nanophotonics* **2015**, *4*, 198.

[40] H. Bryngelsson, M. Stjerndahl, T. Gustafsson, K. Edstr, *J. Power Sources* **2007**, *174*, 970.

[41] F. Shi, A. Pei, D. T. Boyle, J. Xie, X. Yu, X. Zhang, Y. Cui, *Proc. Natl. Acad. Sci.* **2018**, *115*, 8529.

[42] M. D. Tikekar, L. A. Archer, D. L. Koch, *Sci. Adv.* **2016**, *2*, 1600320.

[43] J. K. Stark, Y. Ding, P. A. Kohl, *J. Electrochem. Soc.* **2011**, *158*, A1100.

[44] C. Fang, J. Li, M. Zhang, Y. Zhang, F. Yang, J. Z. Lee, M.-H. Lee, J. Alvarado, M. A. Schroeder, Y. Yang, B. Lu, N. Williams, M. Ceja, L. Yang, M. Cai, J. Gu, K. Xu, X. Wang, Y. S. Meng, *Nature* **2019**, *572*, 511.

[45] J.-H. Cheng, A. A. Assegie, C.-J. Huang, M.-H. Lin, A. M. Tripathi, C.-C. Wang, M.-T. Tang, Y.-F. Song, W.-N. Su, B. J. Hwang, *J. Phys. Chem. C* **2017**, *121*, 7761.

[46] S. van der Walt, J. L. Schönberger, J. Nunez-Iglesias, F. Boulogne, J. D. Warner, N. Yager, E. Gouillart, T. Yu, *PeerJ* **2014**, *2014*, e453.

[47] Y. Métivier, G. Richomme, *J. Power Sources* **1999**, *81–82*, 925.

[48] W. Plieth, *Nucleation and Growth of Metals, chapter of the bookElectrochemistry for Materials Science*, Elsevier, USA **2008**.

[49] X. G. Yang, S. Ge, T. Liu, Y. Leng, C. Y. Wang, *J. Power Sources* **2018**, *395*, 251.

[50] A. Paolella, W. Zhu, G. Xu, A. La Monaca, S. Savoie, G. Girard, A. Vijh, H. Demers, A. Perea, N. Delaporte, A. Guerfi, X. Liu, Y. Ren, C. J. Sun, J. Lu, K. Amine, K. Zaghib, *Adv. Energy Mater.* **2020**, *10*, 2001497.

[51] W. Zhu, H. Demers, G. Girard, D. Clement, F. Zimin, A. Guerfi, M. Trudeau, A. Vijh, A. Paolella, *J. Power Sources* **2022**, *546*, 231941.

[52] S. Kaboli, P. Noel, D. Clément, H. Demers, A. Paolella, P. Bouchard, M. L. Trudeau, J. B. Goodenough, K. Zaghib, *Sci. Adv.* **2020**, eabd5708.

[53] R. T. Pekarek, A. Affolter, L. Baranowski, J. Coyle, T. Hou, E. Sivonxay, B. Smith, R. D. McAuliffe, K. A. Persson, B. Key, C. Apblett, G. M. Veith, N. R. Neale, *J. Mat. Chem. A* **2020**, *8*, 7897.

[54] S. Abramowitz, N. Acquista, I. W. Levin, *J. Res. the Notional Bureau of Stand.-A. Phys. Chem.* **1972**, *1*, 1.

[55] G. V. Zhuang, K. Xu, T. R. Jow, P. N. Ross, *Electrochem. Solid-State Lett.* **2004**, *7*, A224.

[56] S. Grugeon, P. Jankowski, D. Cailleu, C. Forestier, L. Sannier, M. Armand, P. Johansson, S. Laruelle, *J. Power Sources* **2019**, *427*, 77.

[57] F. Shi, P. N. Ross, G. A. Somorjai, K. Komvopoulos, *J. Phys. Chem. C* **2017**, *121*, 14476.

[58] M. Golozar, P. Hovington, A. Paolella, S. Bessette, M. Lagacé, P. Bouchard, H. Demers, R. Gauvin, K. Zaghib, *Nano Lett.* **2018**, *18*, 7583.

[59] G. Weber, E. Sciora, J. Guichard, F. Bouyer, I. Bezverkhyy, J. Marcos Salazar, C. Dirand, F. Bernard, H. Lecoq, R. Besnard, J.-P. Bellat, *J. Therm. Anal. Calorim.* **2018**, *132*, 1055.

[60] G. McConohy, X. Xu, T. Cui, E. Barks, S. Wang, E. Kaeli, C. Melamed, X. W. Gu, W. C. Chueh, *Nat. Energy* **2023**, *8*, 241.

[61] R. Guo, B. M. Gallant, *Chem. Mater.* **2020**, *32*, 5525.

[62] C. Li, X. Guo, L. Gu, D. Samuelis, J. Maier, *Adv. Funct. Mater.* **2011**, *21*, 2901.

[63] J. Pan, Q. Zhang, X. Xiao, Y. T. Cheng, Y. Qi, *ACS Appl. Mater. Interfaces* **2016**, *8*, 5687.

[64] S. Lorger, R. Usiskin, J. Maier, *J. Electrochem. Soc.* **2019**, *166*, A2215.

[65] S. Ssenyange, F. Anariba, D. F. Bocian, R. L. McCreery, *Langmuir* **2005**, *21*, 11105.

[66] K.-H. Chen, K. N. Wood, E. Kazyak, W. S. LePage, A. L. Davis, A. J. Sanchez, N. P. Dasgupta, *J. Mater. Chem. A Mater.* **2017**, *5*, 11671.

[67] S. Kaboli, W. Zhu, D. Clément, M. Dontigny, F. Gendron, K. Amouzegar, A. Guerfi, A. Vijh, M. L. Trudeau, A. Paolella, *ACS Appl. Energy Mater.* **2023**, *6*, 4257.